Supporting Information for the Manuscript

Polyacrylonitrile-Containing Amphiphilic Block Copolymers: Self-Assembly and Porous Membrane Formation

*Lea Gemmer[1], Bart-Jan Niebuur[2], Christian Dietz[3], Daniel Rauber[4], Martina Plank[5], Florian V. Frieß[1], Volker Presser[4,6,7], Robert W. Stark[3], Tobias Kraus[2,8], Markus Gallei[1,7]**

[1] Polymer Chemistry, Universität des Saarlandes, Campus Saarbrücken C4 2, 66123 Saarbrücken, Germany

[2]INM – Leibniz-Institute for New Materials, Campus D2 2, 66123 Saarbrücken, Germany

[3]Physics of Surfaces, Institute of Materials Science, Technische Universität Darmstadt, Peter-Grünberg-Straße 2, 64287 Darmstadt, Germany

[4]Department of Materials Science and Engineering, Saarland University, 66123 Saarbrücken, Germany

[5]Ernst-Berl Institute of Technical and Macromolecular Chemistry, Technische Universität Darmstadt, Peter-Grünberg-Straße 4, 64287 Darmstadt, Germany

[6]INM - Leibniz-Institute for New Materials, Campus D2 2, 66123 Saarbrücken, Germany

[7]Saarene, Saarland Center for Energy Materials and Sustainability, Campus C4 2, 66123 Saarbrücken, Germany

[8]Colloid and Interface Chemistry, Universität des Saarlandes, Campus D2 2, 66123 Saarbrücken, Germany

Synthesis and Characterization of PSAN-*b*-PHEMA

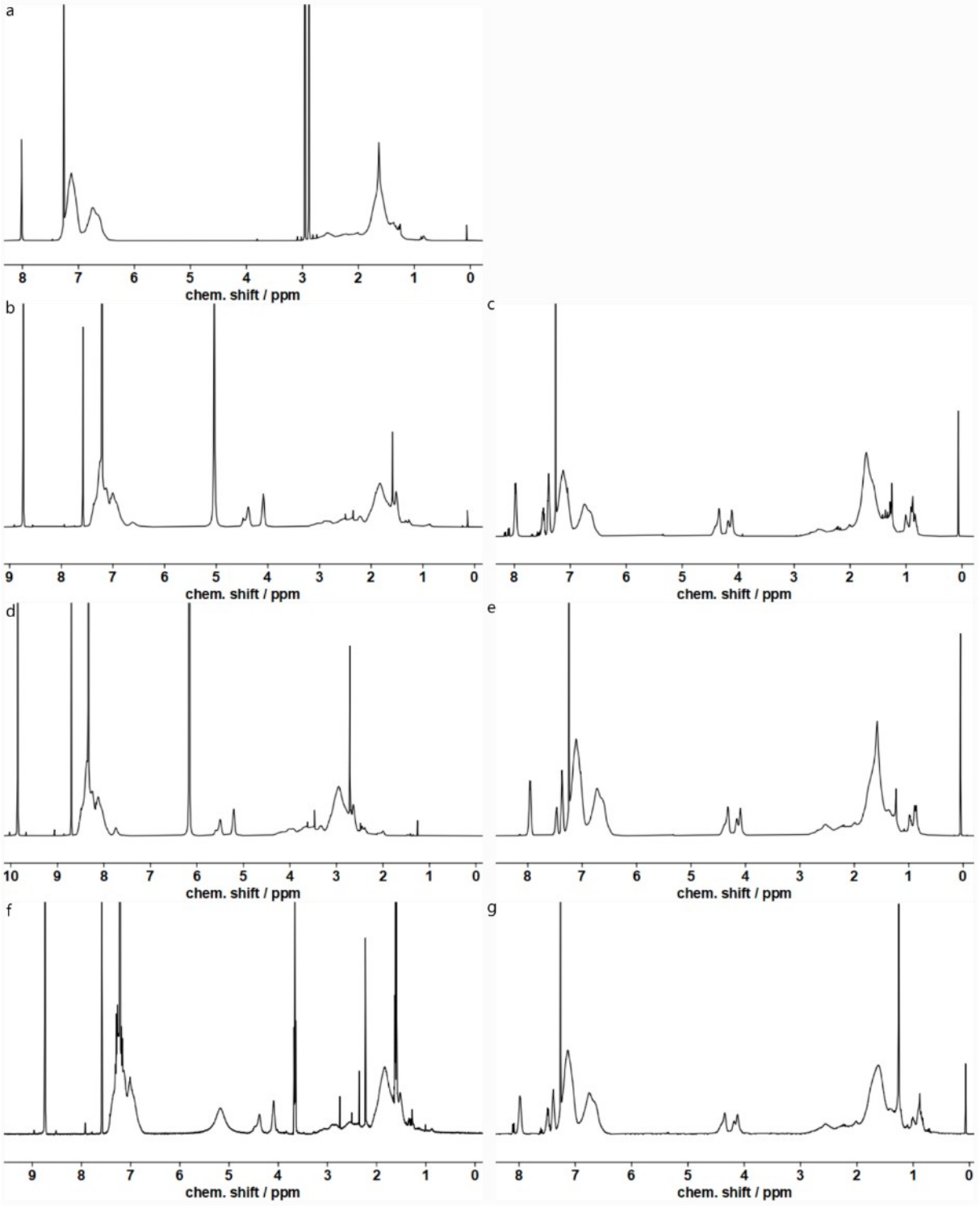

Figure S1: ^{1}H-NMR spectra of the synthesized polymers $PSAN_{738}$ in $CDCl_3$ (a), $PSAN_{83}$-*b*-$PHEMA_{17}^{82}$ in py-d_5 (b) and $PSAN_{83}$-*b*-$PHEMA(\text{-}Bz)_{17}^{82}$ in $CDCl_3$ (c), $PSAN_{87}$-*b*-$PHEMA_{13}^{76}$ in py-d_5 (d) and $PSAN_{87}$-*b*-$PHEMA(\text{-}Bz)_{13}^{76}$ in $CDCl_3$ (e), $PSAN_{88}$-*b*-$PHEMA_{12}^{41}$ in py-d_5 (f) and $PSAN_{88}$-*b*-$PHEMA(\text{-}Bz)_{12}^{41}$ in $CDCl_3$ (g).

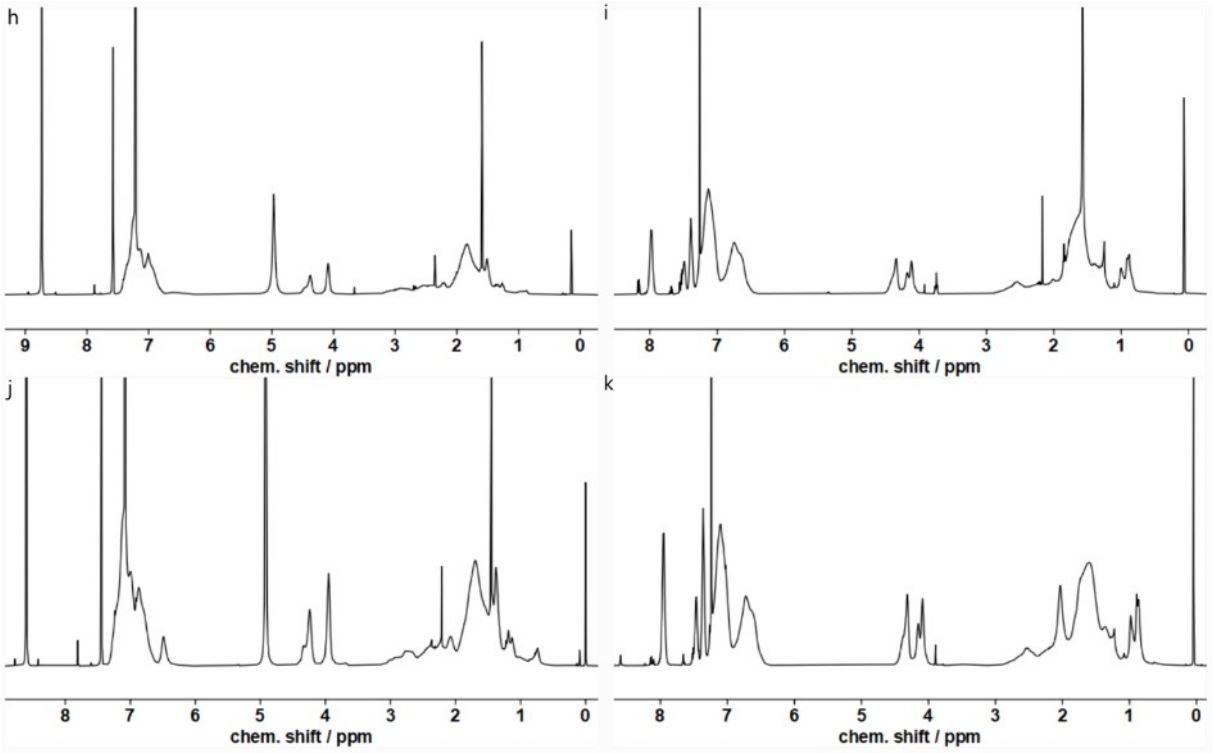

Figure S2: ^{1}H-NMR spectra of the synthesized polymers $PSAN_{84}$-*b*-$PHEMA_{16}^{45}$ in py-d_5 (h) and $PSAN_{84}$-*b*-$PHEMA(\text{-}Bz)_{16}^{45}$ in $CDCl_3$ (i), $PSAN_{80}$-*b*-$PHEMA_{20}^{47}$ in py-d_5 (j) and $PSAN_{80}$-*b*-$PHEMA(\text{-}Bz)_{20}^{47}$ in $CDCl_3$ (k).

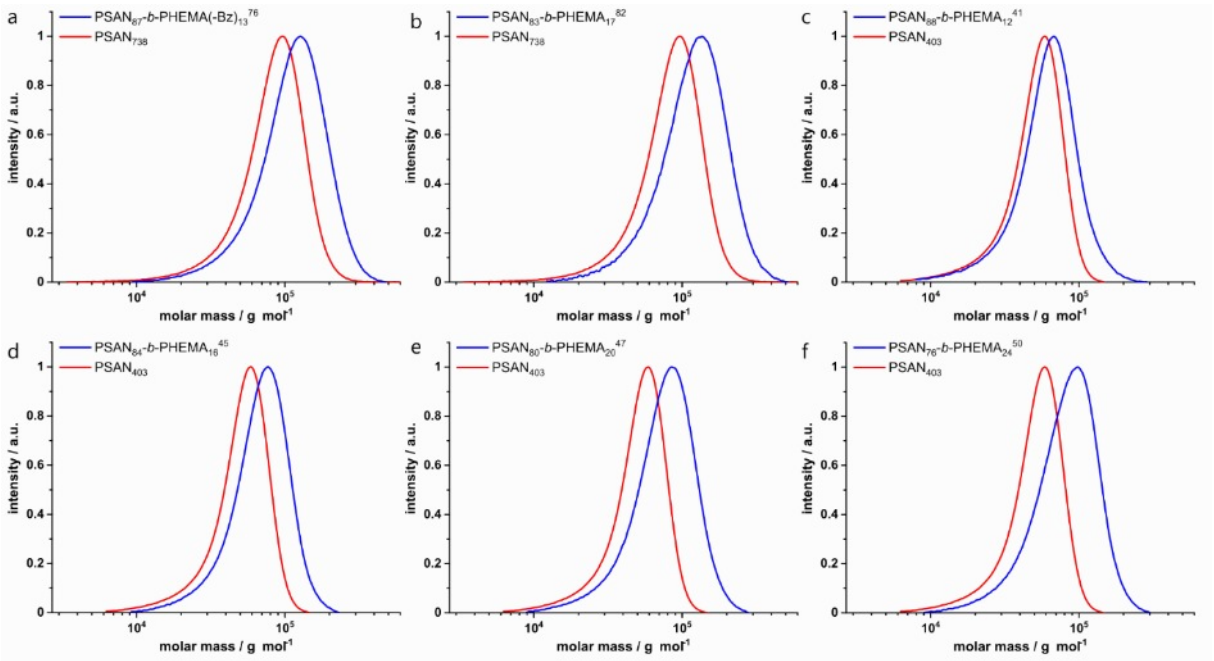

Figure S3: SEC-traces collected in DMF as an eluent with PMMA-standards of the synthesized macroinitiators $PSAN_{738}$ (a, b) and $PSAN_{403}$ (c, d, e, f) in red, and the BCPs $PSAN_{87}$-*b*-$PHEMA_{13}^{76}$ (a) $PSAN_{83}$-*b*-$PHEMA_{17}^{82}$ (b) $PSAN_{88}$-*b*-$PHEMA_{12}^{41}$ (c) $PSAN_{84}$-*b*-$PHEMA_{16}^{45}$ (d) $PSAN_{80}$-*b*-$PHEMA_{20}^{47}$ (e) $PSAN_{76}$-*b*-$PHEMA_{24}^{50}$ (f) in blue.

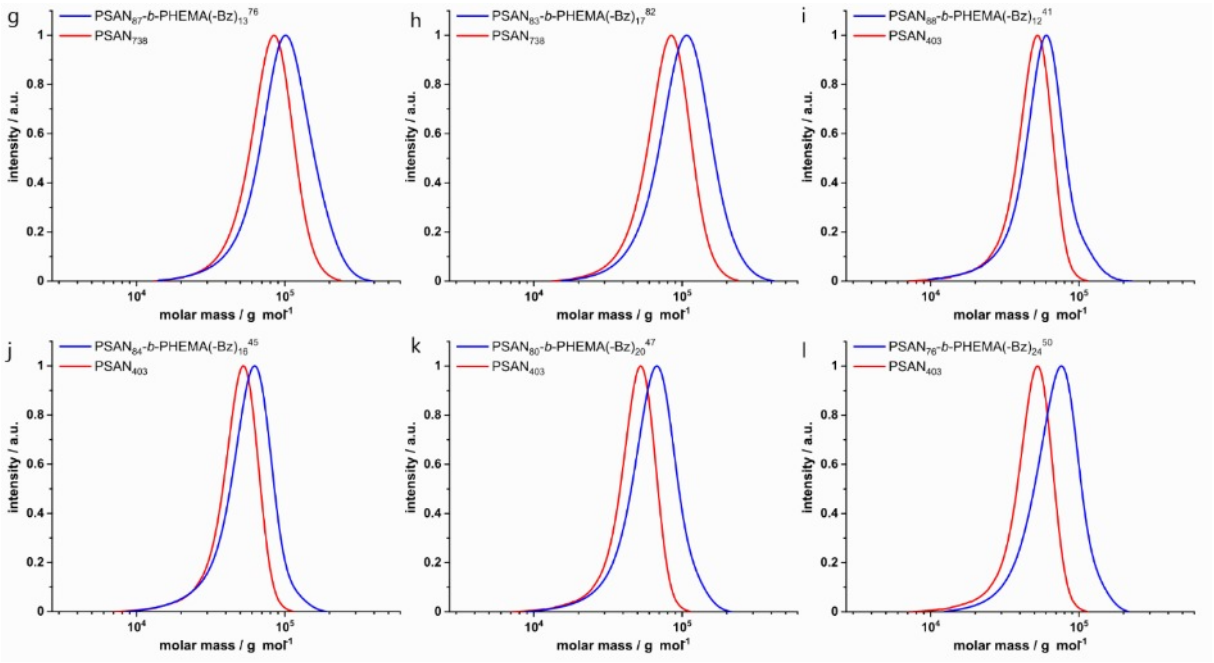

Figure S4: SEC-traces collected in THF as an eluent with PS-standards of the synthesized macroinitiators $PSAN_{738}$ (a, b) and $PSAN_{403}$ (c, d, e, f) in red, and the BCPs $PSAN_{87}$-*b*-$PHEMA(\text{-Bz})_{13}^{76}$ (a) $PSAN_{83}$-*b*-$PHEMA(\text{-Bz})_{17}^{82}$ (b) $PSAN_{88}$-*b*-$PHEMA(\text{-Bz})_{12}^{41}$ (c) $PSAN_{84}$-*b*-$PHEMA(\text{-Bz})_{16}^{45}$ (d) $PSAN_{80}$-*b*-$PHEMA(\text{-Bz})_{20}^{47}$ (e) $PSAN_{76}$-*b*-$PHEMA(\text{-Bz})_{24}^{50}$ (f) in blue.

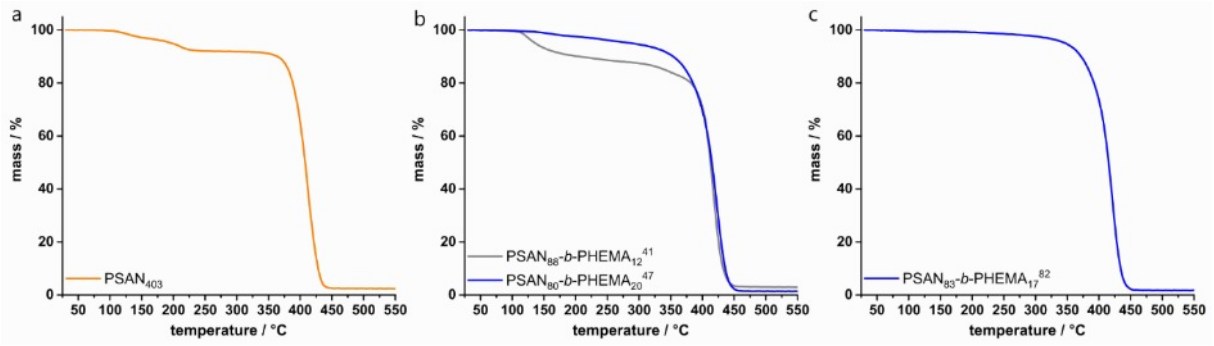

Figure S5: Thermograms from thermogravimetric analysis of the macroinitiator $PSAN_{403}$ (a), and the BCPs $PSAN_{88}$-*b*-$PHEMA_{12}^{41}$ and $PSAN_{80}$-*b*-$PHEMA_{20}^{47}$ (b), and $PSAN_{83}$-*b*-$PHEMA_{17}^{82}$ (c).

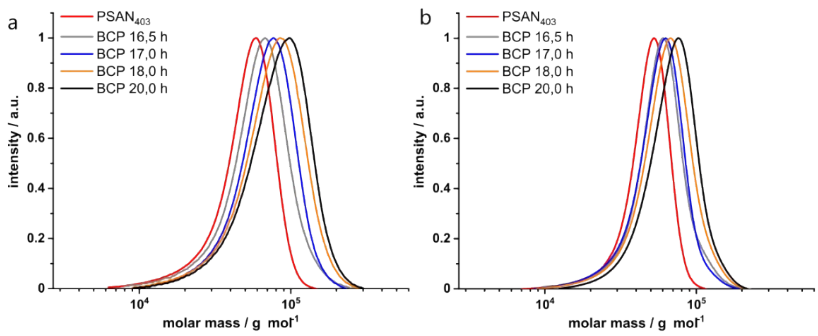

Figure S6: Compiled SEC-traces of the macroinitiator $PSAN_{403}$ (red) and corresponding BCPs by increasing reaction time of the second block in DMF as an eluent with PMMA-standard (a) and in THF as an eluent with PS-standard (b).

Diffusion NMR Investigations

Instrumentation:

Diffusion ordered spectroscopy (DOSY) was conducted on an Avance 500 Neo NMR spectrometer (Bruker) equipped with a Prodigy TCI cryo probe head and a BCU II temperature unit using the ^{1}H nucleus to determine of the diffusion coefficient of the macromolecular segments in solution. For sample preparation 2 mg of the samples were dissolved in deuterated pyridine until a homogenous dissolution was achieved and then placed in 5 mm NMR tubes. Gradient calibration was performed and validated by measuring the self-diffusion coefficient of ultrapure water and comparing to literature values.[1] The samples were placed in the NMR spectrometer and thermally equilibrated to 298.15 K before shimming and locking to the signals from the residual protons of the solvent. Afterwards the pulse width of the 90° pulse and longitudinal relaxation time T_1 were determined. The diffusion coefficients of the BCPs were determined using the ledbpgp2s pulse sequence for the pulsed field gradient stimulated echo experiment (PFGSTE) with bipolar gradient pulses and longitudinal eddy current delay (LED). Before the measurement the set of diffusion time Δ and gradient duration δ were optimized to yield a signal attenuation of 95% when the measurement with the highest applied field gradient was compared to the initial one with low gradient applied. For the measurement gradients from

2 to 95 % of the probe's maximum gradient strength (65.7 G cm^{-1}) were applied. The gradient shape was that of a smoothed rectangular. With the determined parameters, a series of 32 measurements with each 16 scans and linear increase in gradient was conducted. The individual resonances of the high-resolution NMR experiment allowed for the assignment of the diffusion coefficients to specific sites in the macromolecule (see Figure 1). Due to the much faster diffusion of the solvent molecules compared to the polymers, these signals are removed from the spectra for higher gradient strength, effectively filtering them in case of overlap with signals from the macromolecules. The diffusion coefficients D were determined by regression of the Stejskal–Tanner equation (S1)

$$I = I_0 \cdot \exp\left(- D(\gamma\delta g)^2\left(\Delta - \frac{\delta}{3} - \frac{\tau}{2}\right)\right) \quad \text{(S1)}$$

With I the signal intensity of the scan with applied magnetic field gradient, I_0 the initial signal intensity without applied field gradient, D the diffusion coefficient, γ the gyromagnetic ratio of the investigated nucleus (^{1}H), δ the duration of the gradient, g the gradient strength, Δ the diffusion time and the τ gradient interspacing. The diffusion coefficients of the individual signal were obtained by plotting the signal intensity with increasing gradient strength in dependence of the fixed experimental parameters (summarized as Q-value), equation (S2).

$$I = I_0 \cdot \exp\left(- DQ\right) \quad \text{(S2)}$$

All signals of both the macroinitiator and the BCP could be well fitted using a monoexponential function, indicating a narrow and symmetric molecular weight distribution. An uncertainty of ≈ 2 % for the diffusion coefficients was estimated from repeated measurements, comparison to literature values for other systems and variation of experimental parameters.

Evaluation:

Diffusion-ordered spectroscopy (DOSY) is an advanced NMR method that allows the assignment of NMR signals to different species according to their diffusion coefficient. A macroinitiator featuring a smaller hydrodynamic volume usually has a higher diffusion

coefficient than the block copolymer built from it. These species could therefore be distinguished by diffusion NMR. Two samples were measured in solutions of diluted pyridine-d_5, namely the macroinitiator $PSAN_{403}$ and the BCP $PSAN_{80}$-*b*-$PHEMA_{20}$[47].

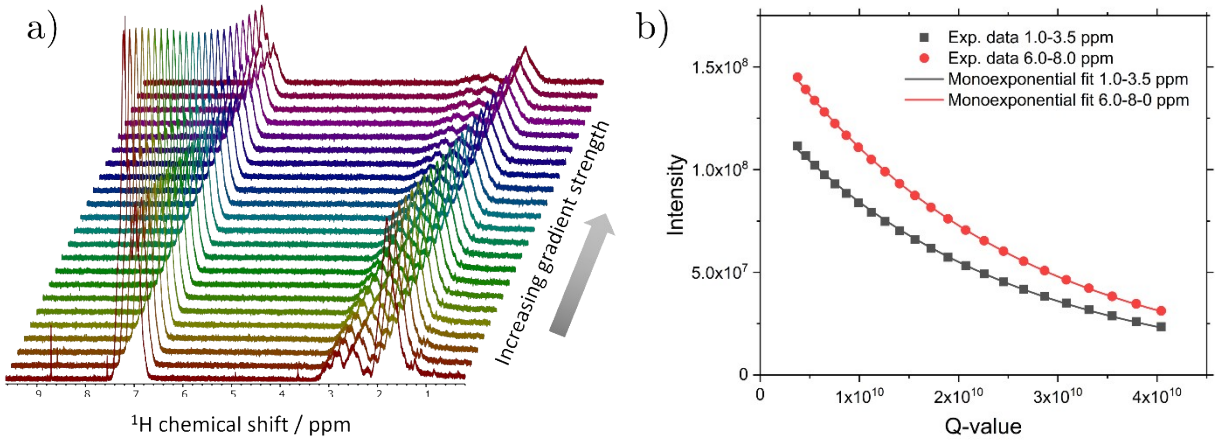

Figure S7: Diffusion measurement (PFGSTE) of macroinitiator $PSAN_{403}$. a) Stacked-plot representation showing the decrease in signal intensity with increasing gradient strength. b) Plot of the intensity *vs.* Q-value according to the Stejskal–Tanner equation (S1) for the given spectral ranges and monoexponential fits to derive the diffusion coefficients (D(1.0-3.5 ppm) = 4.25×10^{-11} m^2 s^{-1}; D(6.0-8.0 ppm) = 4.18×10^{-11} m^2 s^{-1}).

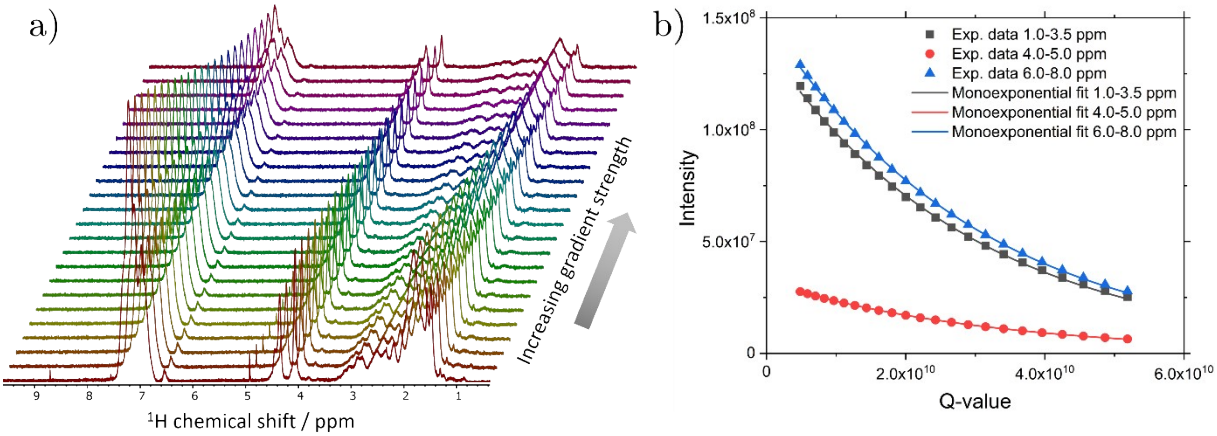

Figure S8: Diffusion measurement (PFGSTE) of BCP $PSAN_{80}$-*b*-$PHEMA_{20}$[47]. a) Stacked-plot representation showing the decrease in signal intensity with increasing gradient strength. b) Plot of the intensity *vs.* Q-value according to the Stejskal–Tanner equation (S1) for the given spectral ranges and monoexponential fits to derive the diffusion coefficients (D(1.0-3.5 ppm = 3.33×10^{-11} m^2 s^{-1}; D(4.0-5.0 ppm) = 3.12×10^{-11} m^2 s^{-1}; D(6.0-8.0 ppm) = 3.30×10^{-11} m^2 s^{-1}).

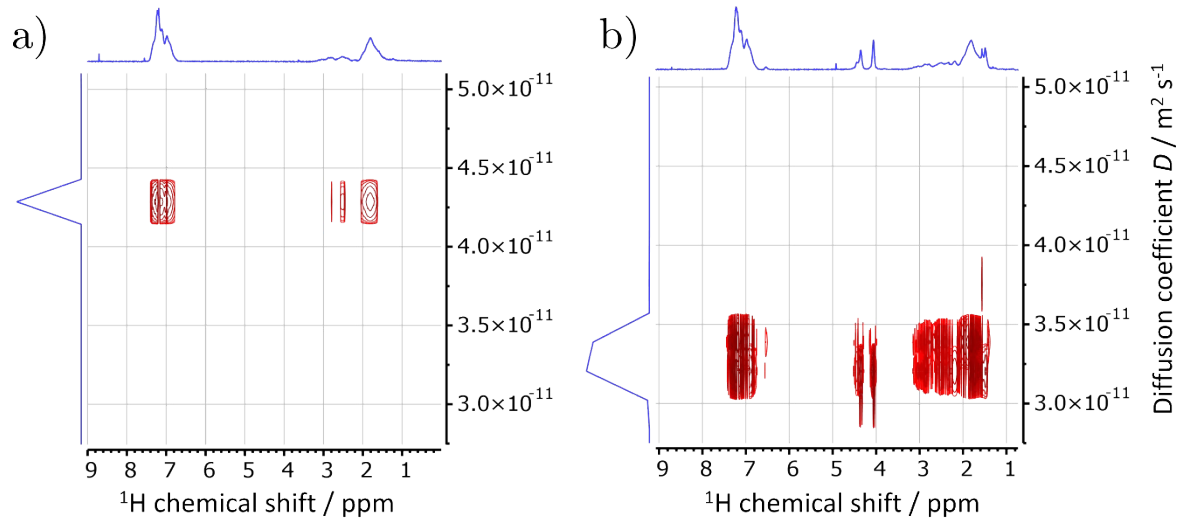

Figure S9: Diffusion ordered spectroscopy (DOSY) plot of a) the macroinitiator $PSAN_{403}$ and b) the BCP $PSAN_{80}$-*b*-$PHEMA_{20}^{47}$ showing the slower diffusion of the BCP and the approximately equal diffusion coefficients *D* for all three blocks of the copolymer. This indicates a successful polymerization as shown by the weight increase (lower *D* of BCP $PSAN_{80}$-*b*-$PHEMA_{20}^{47}$) and a low amount of unreacted macroinitiator.

Microphase Separation of PSAN-*b*-PHEMA in the Bulk State

SAXS model for randomly close packed spheres

It is given by the function

$$I(q) = S_{HS}(q)P_{pS}(q) \quad \text{(S3)}$$

with $P_{pS}(q)$ is the form factor of polydisperse spheres following a Gaussian size distribution, which gives the radius R of the nanoparticles and the width of the distribution, σ,[2] and $S_{HS}(q)$ a disordered hard-sphere structure factor, accounting for the nanoparticle arrangement. It yields the hard sphere radius, R_{HS}, i.e., half of the center-to-center distance between the spheres, and the volume fraction that the hard spheres occupy within the agglomerates, η.[3]

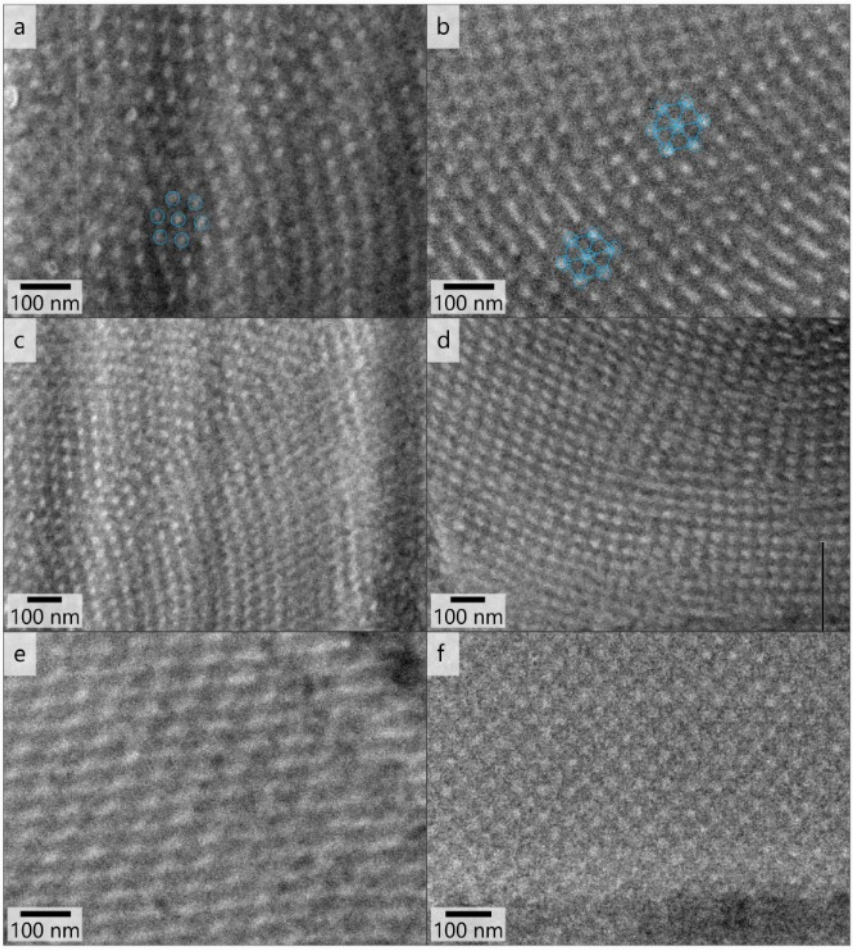

Figure S10: Bulk morphology investigations via TEM of thin slices of BCPs $PSAN_{80}$-*b*-$PHEMA_{20}$[47] (a, compare to Figure 3 d) $PSAN_{76}$-*b*-$PHEMA_{24}$[50] (b, compare to Figure 3 g) with visible hexagonal structures highlighted in blue. Areas with apparently bicontinuous

morphologies of BCP $PSAN_{80}$-*b*-$PHEMA_{20}$[47] (c, d) and $PSAN_{76}$-*b*-$PHEMA_{24}$[50] (e, f) are shown.

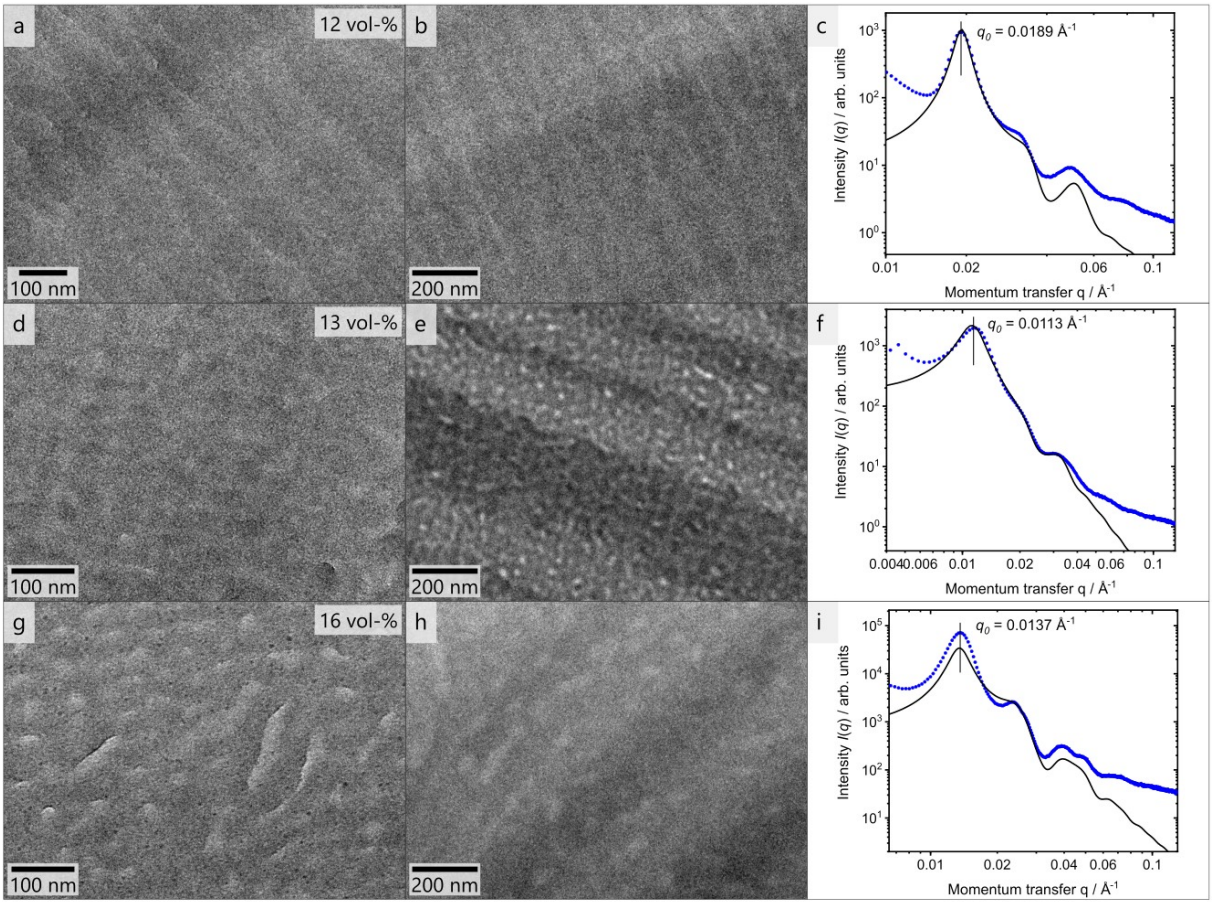

Figure S11: Bulk morphology investigations via TEM of thin slices of BCPs $PSAN_{88}$-*b*-$PHEMA_{12}$[41] (a, b), $PSAN_{87}$-*b*-$PHEMA_{13}$[76] (d, e), $PSAN_{84}$-*b*-$PHEMA_{16}$[45] (g, h) in two magnifications, with corresponding SAXS curves in blue dots and model plots, following equation (1) in the main text, in black lines (c, f, i). The PHEMA-volume fractions of the samples shown in each row are depicted.

Discussion to Figure S11:

The BCP $PSAN_{88}$-*b*-$PHEMA_{12}$[41] does not reveal distinct microphases in transmission electron micrographs (Figure S11 a and b) but SAXS (Figure S11 c) indicates the formation of a microphase separated structure. The scattering pattern is compared to that of randomly close packed spheres (equation (1) in the main text) with a sphere size (R) of 11.7 nm, a width of the radius distribution (σ) of 1.3 nm and a sphere center-to-center distance of 36.7 nm showing a qualitative agreement between data and model. It can be concluded that this structure dominates

in the sample, but the presence of additional structures cannot be excluded. The BCPs $PSAN_{87}$-*b*-$PHEMA_{13}^{76}$ (d-f) and $PSAN_{84}$-*b*-$PHEMA_{16}^{45}$ (g-i) exhibit distinct but apparently non-ordered microphases in the transmission electron micrographs, but the SAXS patterns suggest a structure consisting of randomly close packed spheres, as follows from the comparison with the model for both samples. For $PSAN_{87}$-*b*-$PHEMA_{13}^{76}$ the models estimated a sphere size of 17.3 nm with σ = 2.8 nm and a sphere center-to-center distance of 36.8 nm, whereas for $PSAN_{84}$-*b*-$PHEMA_{16}^{45}$ R = 13.0 nm with σ = 1.5 nm, and a sphere center-to-center distance of 25.0 nm. It should be noted, however, that deviations between the data and the model exist in both cases.

Variations between SAXS and TEM can occur due to impacts of the preparation of thin slices and contrasting agent reactions. Moreover, TEM only gives a local fraction of the film, while in SAXS larger volumes are probed.

Table S1. Comparison of domain sizes of BCPs with similar compositions and molar masses according to their flory interaction parameter $\chi_{A/B}$.

Polymer	$M_{n,\,ges,\,cal}$ / kDa	$\Phi_{2nd\ block}$ / vol%	D_{SAXS} / nm	reference	$\chi_{A/B}$
PS-*b*-PB	56	28	38	76	0.06 [4]
PS-*b*-PHEMA	58	24	46	76	0.37 [5]
PSAN-*b*-PHEMA	50	24	52	this work	-

Micelle formation of PSAN and PSAN-*b*-PHEMA

Exemplary preparation of micelles in THF/DMF 2:3

In a rolled rim bottle 1.2 mg of polymer powder was dissolved in 2.3 mL of DMF by stirring with a magnetic stirring bar. After complete dissolution, 1.7 mL of THF were added dropwise to the polymer solution. The solution was subsequently diluted by serial dilution with a mixture of THF/DMF 2:3 (v/v) in multiple steps until a concentration of 0.001 mg mL^{-1} was obtained. One drop of the solution was placed on a copper grid to dry over night for TEM analysis.

Results and discussion

The solvents THF, dioxane (DOX), DMF and *N*-methyl pyrrolidone (NMP) were chosen. Micelles in solution were prepared from the respective mixtures (i) THF/DMF/DOX 2:1:1 and (ii) THF/DMF/DOX 3:1:1 and (iii) THF/NMP/DOX 3:1:1. In Figure S12 the corresponding micelles of the two exemplary polymers $PSAN_{88}$-*b*-$PHEMA_{12}^{41}$ and $PSAN_{80}$-*b*-$PHEMA_{20}^{47}$ in mixtures (i) and (iii) are shown. A broader overview including imprinted average micelle sizes can be found in Figure S13.

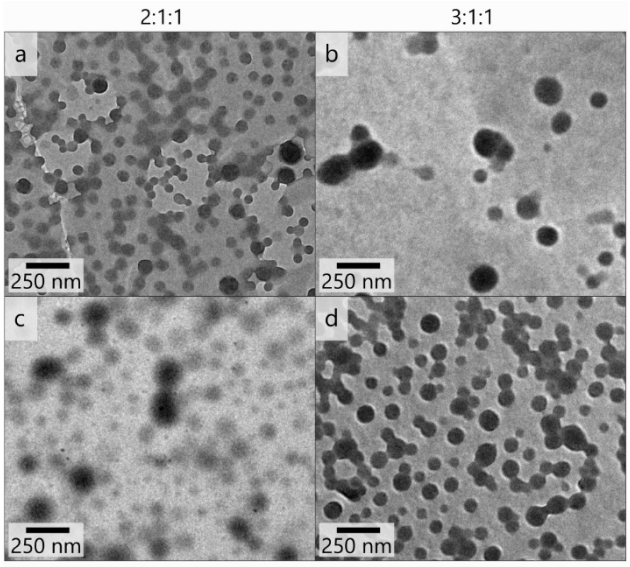

Figure S12. TEM-images of micelle solutions prepared from (i) THF/DMF/DOX 2:1:1 with polymer $PSAN_{88}$-*b*-$PHEMA_{12}^{41}$ (a) and $PSAN_{80}$-*b*-$PHEMA_{20}^{47}$ (c), and from (ii) THF/DMF/DOX 3:1:1 with polymer $PSAN_{88}$-*b*-$PHEMA_{12}^{41}$ (b) and $PSAN_{80}$-*b*-$PHEMA_{20}^{47}$ (d).

The polymer $PSAN_{88}$-*b*-$PHEMA_{12}^{41}$ featuring 12 vol-% of PHEMA exhibited uniform micelles and bigger micelles similarly in the 2:1:1 (i) and 3:1:1 (ii) THF/DMF/DOX-mixture. The micelles obtained from mixture (i) revealed a smaller mean diameter of (68 ± 26) nm than those obtained from mixture (ii) featuring (123 ± 34) nm. Micelles were obtained in both solvent mixtures using the polymer $PSAN_{80}$-*b*-$PHEMA_{20}^{47}$ featuring 20 vol-% of PHEMA. However, the mixture 3:1:1 (ii) revealed the most uniform and distinct micelles featuring a mean diameter of (94 ± 21) nm compared to the mean diameter of (100 ± 47) nm observed in mixture (i). Using mixture (ii), interconnected micelles were also observed, which are presented in Figure S13.

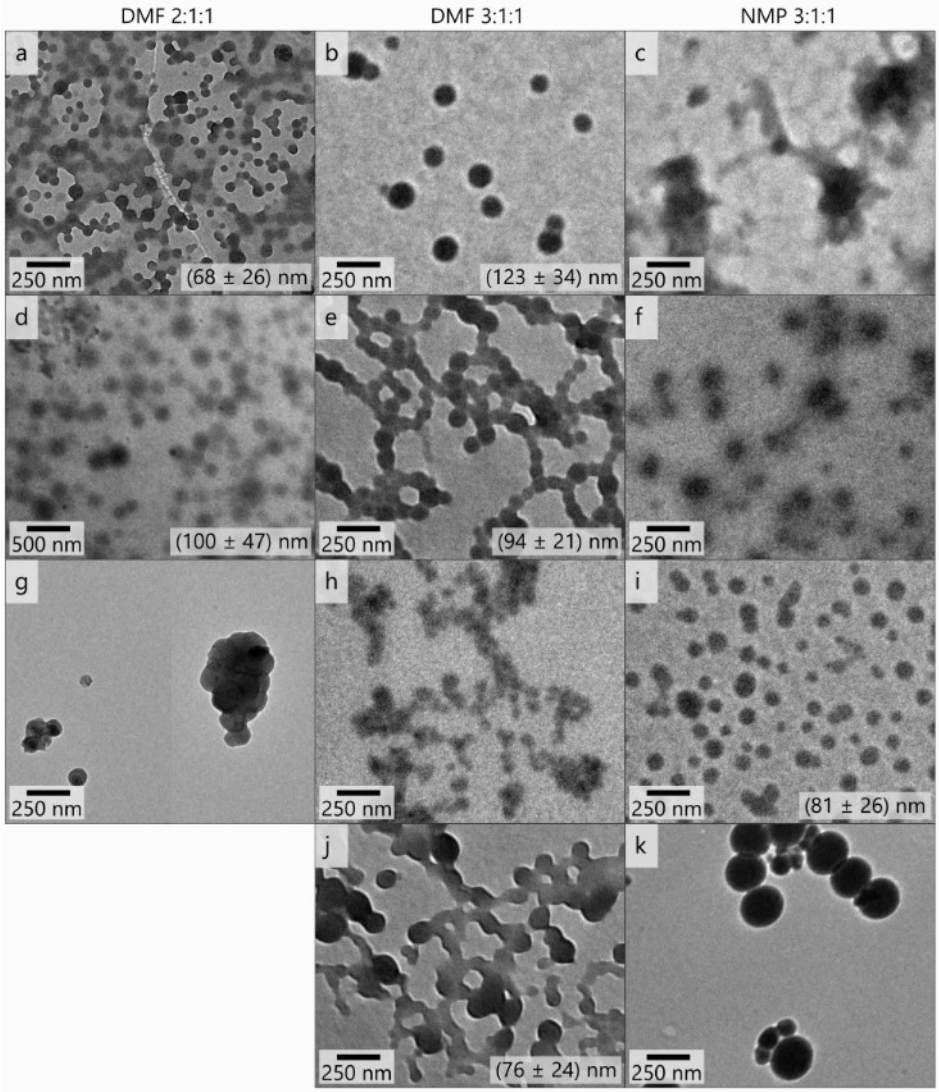

Figure S13. TEM-images of diluted BCP micelle solutions with imprinted micelle diameters (measured with ImageJ), if determinable. Presented are the BCPs $PSAN_{88}$-*b*-$PHEMA_{12}^{41}$ (a-c, also in Figure 4 a, b), $PSAN_{80}$-*b*-$PHEMA_{20}^{47}$ (d-f, also in Figure 4 c, d), $PSAN_{76}$-*b*-$PHEMA_{24}^{50}$

(g-i), and $PSAN_{738}$ (j, k). The images below each other are prepared from the solvent mixture listed above.

The macroinitiator $PSAN_{738}$ formed interconnected micelles when introduced to the solvent mixture (ii) (Figure S13). These findings imply that the copolymer PSAN alone, representing the first block segment in the BCPs, could to self-assemble into microstructures.

Block copolymer membranes of PSAN-*b*-PHEMA

When increasing the THF content of the solvent mixture of the casting solution of $PSAN_{83}$-*b*-$PHEMA_{17}^{82}$ from 2:1:1 (Fig. 5 d) to 3:1:1 (Fig. 5 f), the pore structure appears even more homogeneous and ordered, and fewer large pores were observed. Especially in deeper cavities (Figure S14 a, upper right) very large, non-uniform and non-ordered pores were present. This was found for the membrane cast with the 200 µm blade gap (Figure S14 a, b) and also, but significantly less, for the membrane cast with the 100 µm blade gap (c, d), both at the 2:1:1 composition. These flaws were not found for the membrane cast with the 100 µm blade gap at the 3:1:1 composition (e, f).

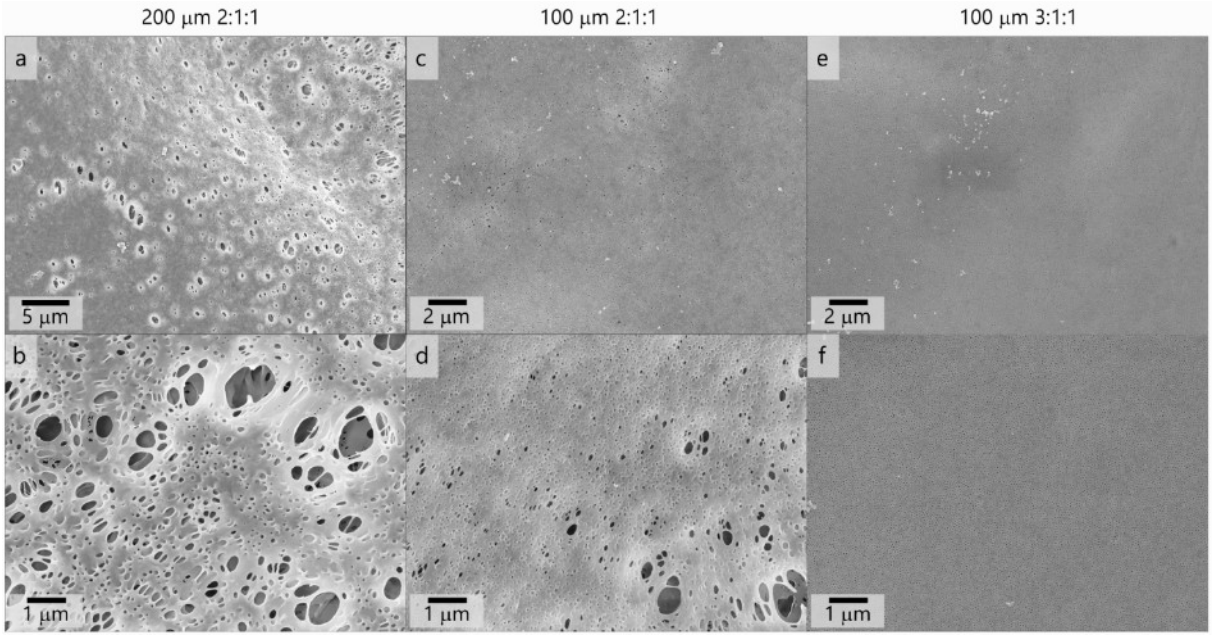

Figure S14. Topography images by SEM of the membrane surfaces cast from solutions of $PSAN_{83}$-*b*-$PHEMA_{17}^{82}$ in THF/DMF/DOX 2:1:1 (a-d) and 3:1:1 (e, f) at 20.3 – 20.5 mass%

using 200 µm (a, b) and 100 µm (c-f) blade gap, representing larger areas (top row) and magnifications (bottom row) of characteristic flaws found in the samples. Please note that the images shown in the main script (Figure 5) represent the greater part of the samples.

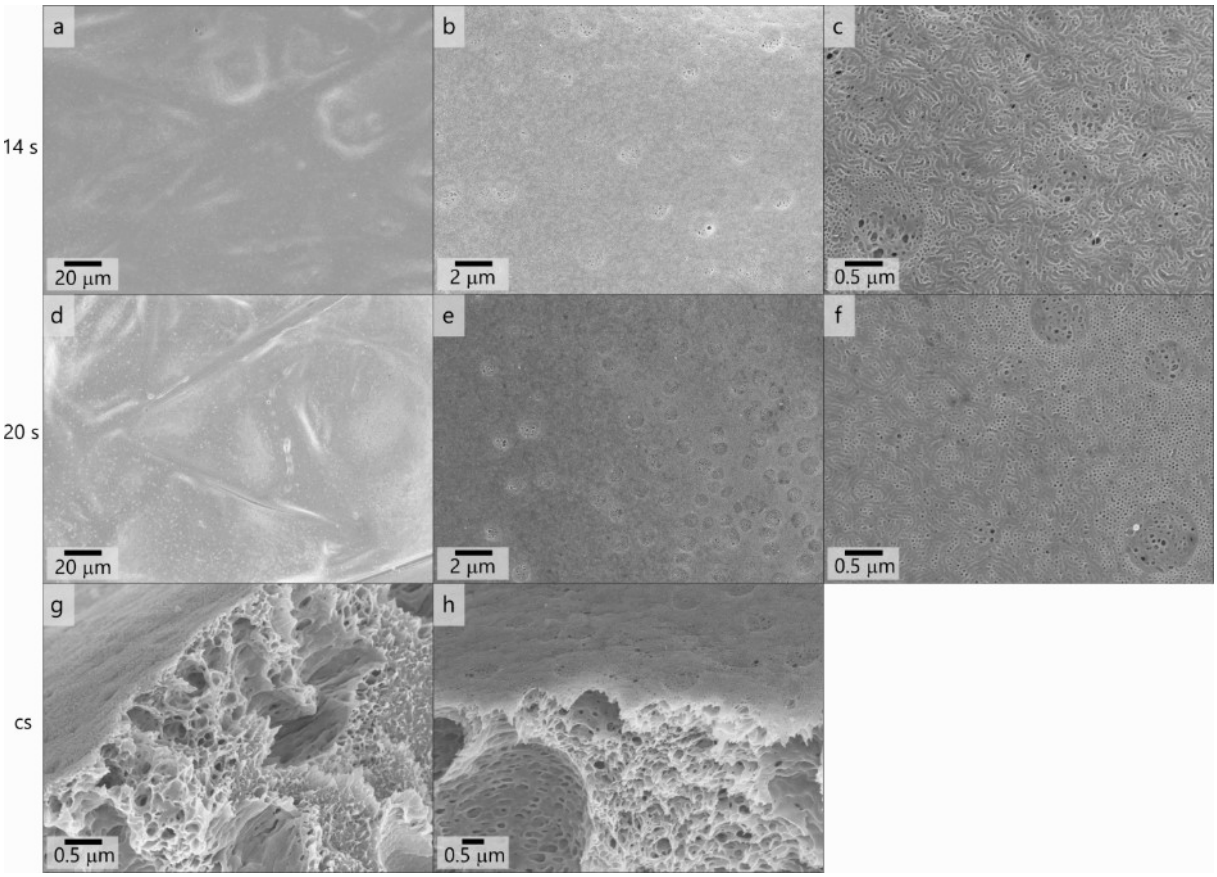

Figure S15. Topography images by SEM of the membrane surfaces cast from solutions of $PSAN_{84}$-*b*-$PHEMA_{16}^{45}$ in THF/DMF/DOX 3:1:1 using the 100 µm blade gap at 24.0 mass% with an evaporation time of 14 s (a-c, g) and 20 s (d-f, h).

Permeance measurements

For the water permeance measurements a 1.5 x 1.5 cm membrane sample was conditioned in ultra-pure water, with a resistance of at least 19 MΩ, for 30 min. The measurement was carried out at 0.2 – 1 bar trans membrane pressure in a dead-end filtration cell. Three samples were collected over 10 min, after a further conditioning period of 1 h at measurement pressure. The values given in Table S2 represent the mean value of these measurements.

Table S2: Mean values of the water permeance for the neat BCP membranes, as well as the plasma cleaned ones. Measurements were carried out using a dead-end filtration cell and ultra-pure water of resistance of at least 19 MΩ.

Sample	Permeance / L m^{-2} h^{-1} bar^{-1}	
	before	after
$PSAN_{83}$-*b*-$PHEMA_{17}^{82}$	3	6583
$PSAN_{84}$-*b*-$PHEMA_{16}^{45}$	3	23 000
PS-b-P4VP (30nm)	350	

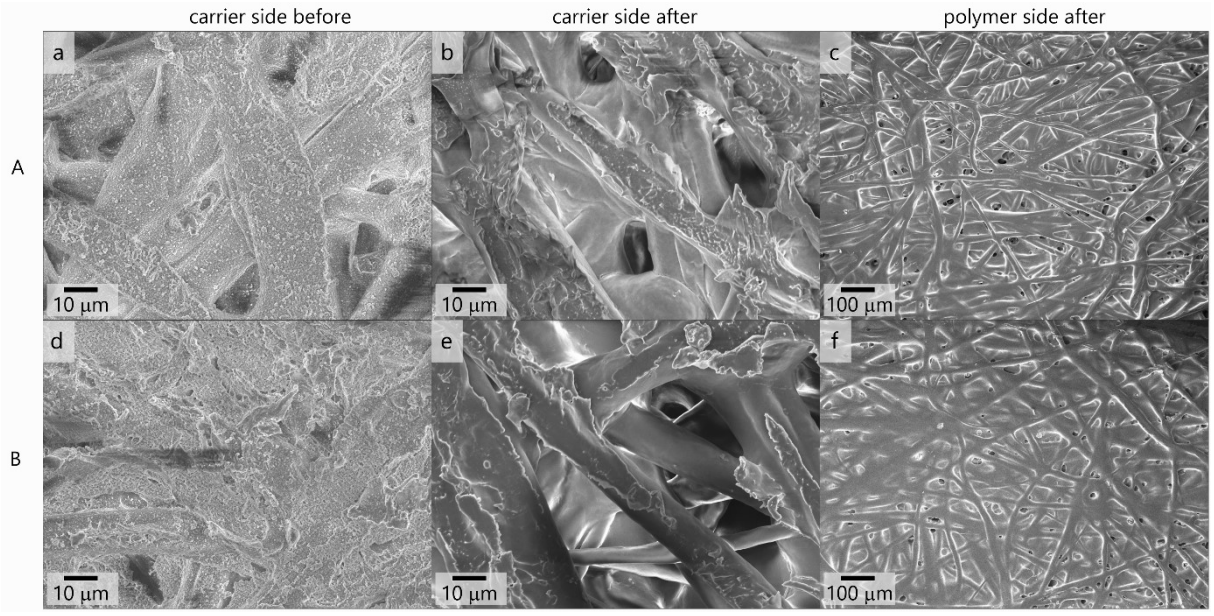

Figure S16. Topography images by SEM of the membranes cast from solutions of $PSAN_{83}$-*b*-$PHEMA_{17}^{82}$ in THF/DMF/DOX 3:1:1 with an evaporation time of 14 s (A) and $PSAN_{84}$-*b*-$PHEMA_{16}^{45}$ in THF/DMF/DOX 3:1:1 with an evaporation time of 20 s (B), comparing the carrier side before (a, d) and after (b, e) treatment with plasma for 1 min, as well as the polymer side (c, f) after the treatment.

Measurable water permeance of the neat BCP membranes verifies their principal porosity. Further SEM investigations reveal a polymer film at the carrier side of the membranes (Figure S16 a and d), which is theorized to be the reason for the low absolute values of permeance. Therefore, we treated the carrier side with plasma for 1 min (Figure S16 b and e). The resulting membranes exhibit very high permeances, while the SEM micrographs show some macro pore formation on the polymer side (Figure S16 c and f). In conclusion we were able to show the general porosity of the presented membranes, while optimization of the parameters for casting are subject to ongoing investigations. To achieve high water fluxes on a mechanically more stable membrane will be part of our future works.

1. A. J. Easteal, W. E. Price and L. A. Woolf, *Journal of the Chemical Society, Faraday Transactions 1: Physical Chemistry in Condensed Phases*, 1989, **85**.
2. P. L. T. Zemb, North Holland, Neutrons, X-rays and light. Scattering methods applied to soft condensed matter.
3. J. K. Percus and G. J. Yevick, *Physical Review*, 1958, **110**, 1-13.
4. V. Balsamo, F. Von Gyldenfeldt and R. Stadler, *Macromolecules*, 1999, **32**, 1226-1232.
5. J. Cheng, R. A. Lawson, W.-M. Yeh, N. D. Jarnagin, L. M. Tolbert and C. L. Henderson, 2013.